

Self-referenced ultra-broadband transient terahertz spectroscopy using air-photonics

F. D'Angelo,¹ H. Němec,² S. H. Parekh,¹ P. Kužel,² M. Bonn,¹ and D. Turchinovich^{1,*}

¹Max Planck Institute for Polymer Research, Ackermannweg 10, 55128, Mainz, Germany

²Institute of Physics, Academy of Sciences of the Czech Republic, Na Slovance 2, 182 21 Prague 8, Czech Republic

*turchino@mpip-mainz.mpg.de

Abstract: Terahertz (THz) air-photonics employs nonlinear interactions of ultrashort laser pulses in air to generate and detect THz pulses. As air is virtually non-dispersive, the optical-THz phase matching condition is automatically met, thus permitting the generation and detection of ultra-broadband THz pulses covering the entire THz spectral range without any gaps. Air-photonics naturally offers unique opportunities for ultra-broadband transient THz spectroscopy, yet many critical challenges inherent to this technique must first be resolved. Here, we present explicit guidelines for ultra-broadband transient THz spectroscopy with air-photonics, including a novel method for self-referenced signal acquisition minimizing the phase error, and the numerically-accurate approach to the transient reflectance data analysis.

© 2016 Optical Society of America

OCIS codes: (300.6495) Spectroscopy, terahertz; (320.7150) Ultrafast spectroscopy; (300.6500) Spectroscopy, time-resolved.

References and links

1. D. Grischkowsky, S. Keiding, M. V. Exter, and C. Fattinger, Far-infrared time-domain spectroscopy with terahertz beams of dielectrics and semiconductors, *J. Opt. Soc. Am. B* **7**, 2006–2015 (1990).
2. P. U. Jepsen, D. G. Cooke, and M. Koch, Terahertz spectroscopy and imaging – modern techniques and applications, *Laser Photon. Rev.* **5**, 124–166 (2011).
3. R. Ulbricht, E. Hendry, J. Shan, T. F. Heinz, and M. Bonn, Carrier dynamics in semiconductors studied with time-resolved terahertz spectroscopy, *Rev. Mod. Phys.* (2011).
4. D. J. Cook and R. M. Hochstrasser, Intense terahertz pulses by four-wave rectification in air, *Opt. Lett.* **25**, 1210–1212 (2000).
5. N. Karpowicz, J. Dai, X. Lu, Y. Chen, M. Yamaguchi, H. Zhao, X.-C. Zhang, L. Zhang, C. Zhang, M. Price-Gallagher, C. Fletcher, O. Mamer, A. Lesimple, and K. Johnson, Coherent heterodyne time-domain spectrometry covering the entire terahertz gap, *Appl. Phys. Lett.* **92**, 011131 (2008).
6. K. Y. Kim, A. J. Taylor, J. H. Glowonia, and G. Rodriguez, Coherent control of terahertz supercontinuum generation in ultrafast laser-gas interactions, *Nat. Photonics* **2**, 605–609 (2008).
7. N. Karpowicz, X. Lu, and X.-C. Zhang, Terahertz gas photonics, *J. Mod. Opt.* **56**, 1137–1150 (2009).
8. X. Lu and X.-C. Zhang, Investigation of ultra-broadband terahertz time-domain spectroscopy with terahertz wave gas photonics, *Front. Optoelectron.* **7**, 121–155 (2014).
9. K. Y. Kim, J. H. Glowonia, A. J. Taylor, and G. Rodriguez, Terahertz emission from ultrafast ionizing air in symmetry-broken laser fields, *Opt. Express* **15**, 4577–4584 (2007).
10. P. Klarskov, A. C. Strikwerda, K. Iwaszczuk, and P. U. Jepsen, Experimental three-dimensional beam profiling and modeling of a terahertz beam generated from a two-color air plasma, *New J. Phys.* **15**, 075012 (2013).

11. F. Buccheri and X.-C. Zhang, Terahertz emission from laser-induced microplasma in ambient air, *Optica* **2**, 366–369 (2015).
12. J. Liu and X. C. Zhang, Birefringence and absorption coefficients of alpha barium borate in terahertz range, *J. Appl. Phys.* **106**, 023107 (2009).
13. F. D'Angelo, Z. Mics, M. Bonn, and D. Turchinovich, Ultra-broadband THz time-domain spectroscopy of common polymers using THz air photonics, *Opt. Express* **22**, 12475–12485 (2014).
14. N. Vieweg, B. M. Fischer, M. Reuter, P. Kula, R. Dabrowski, M. A. Celik, G. Frenking, M. Koch, and P. U. Jepsen, Ultrabroadband terahertz spectroscopy of a liquid crystal, *Opt. Express* **20**, 28249–28256 (2012).
15. I.-C. Ho, X. Guo, and X.-C. Zhang, Design and performance of reflective terahertz air-biased-coherent-detection for time-domain spectroscopy, *Opt. Express* **18**, 2872–2883 (2010).
16. D. G. Cooke, F. C. Krebs, and P. U. Jepsen, Direct observation of sub-100 fs mobile charge generation in a polymer-fullerene film, *Phys. Rev. Lett.* **108**, 056603 (2012).
17. D. G. Cooke, A. Meldrum, and P. Uhd Jepsen, Ultrabroadband terahertz conductivity of Si nanocrystal films, *Appl. Phys. Lett.* **101**, 211107 (2012).
18. D. G. Cooke, P. U. Jepsen, J. Y. Lek, Y. M. Lam, F. Sy, and M. M. Dignam, Picosecond dynamics of internal exciton transitions in CdSe nanorods, *Phys. Rev. B* **88**, 241307 (2013).
19. D. A. Valverde-Chávez, C. S. Ponceca, C. C. Stoumpos, A. Yartsev, M. G. Kanatzidis, V. Sundström, and D. G. Cooke, Intrinsic femtosecond charge generation dynamics in single crystal $\text{CH}_3\text{NH}_3\text{PbI}_3$, *Energy Environ. Sci.* **8**, 3700–3707 (2015).
20. T. I. Jeon and D. Grischkowsky, Observation of a Cole-Davidson type complex conductivity in the limit of very low carrier densities in doped silicon, *Appl. Phys. Lett.* **72**, 2259–2261 (1998).
21. S. C. Howells and L. A. Schlie, Transient terahertz reflection spectroscopy of undoped InSb from 0.1 to 1.1 THz, *Appl. Phys. Lett.* **69**, 550 (1996).
22. A. Pashkin, M. Porer, M. Beyer, K. W. Kim, A. Dubroka, C. Bernhard, X. Yao, Y. Dagan, R. Hackl, A. Erb, J. Demsar, R. Huber, and A. Leitenstorfer, Femtosecond response of quasiparticles and phonons in superconducting $\text{YBa}_2\text{Cu}_3\text{O}_{7-\delta}$ studied by wideband terahertz spectroscopy, *Phys. Rev. Lett.* **105**, 067001 (2010).
23. K. W. Kim, A. Pashkin, H. Schäfer, M. Beyer, M. Porer, T. Wolf, C. Bernhard, J. Demsar, R. Huber, and A. Leitenstorfer, Ultrafast transient generation of spin-density-wave order in the normal state of BaFe_2As_2 driven by coherent lattice vibrations, *Nat. Mater.* **11**, 497–501 (2012).
24. L. Thrane, R. H. Jacobsen, P. Uhd Jepsen, and S. R. Keiding, THz reflection spectroscopy of liquid water, *Chem. Phys. Lett.* **240**, 330–333 (1995).
25. T.-I. Jeon and D. Grischkowsky, Characterization of optically dense, doped semiconductors by reflection THz time domain spectroscopy, *Appl. Phys. Lett.* **72**, 3032 (1998).
26. A. Pashkin, M. Kempa, H. Němec, F. Kadlec, and P. Kužel, Phase-sensitive time-domain terahertz reflection spectroscopy, *Rev. Sci. Instrum.* **74**, 4711 (2003).
27. H. Zhong, C. Zhang, L. Zhang, Y. Zhao, and X.-C. Zhang, A phase feature extraction technique for terahertz reflection spectroscopy, *Appl. Phys. Lett.* **92**, 221106 (2008).
28. S. Nashima, O. Morikawa, K. Takata, and M. Hangyo, Measurement of optical properties of highly doped silicon by terahertz time domain reflection spectroscopy, *Appl. Phys. Lett.* **79**, 3923–3925 (2001).
29. C. Kadlec, V. Skoromets, F. Kadlec, H. Němec, J. Hlinka, J. Schubert, G. Panaitov, and P. Kužel, Temperature and electric field tuning of the ferroelectric soft mode in a strained $\text{SrTiO}_3/\text{DyScO}_3$ heterostructure, *Phys. Rev. B* **80**, 174116 (2009).
30. K. Iwaszczuk, D. G. Cooke, M. Fujiwara, H. Hashimoto, and P. U. Jepsen, Simultaneous reference and differential waveform acquisition in time-resolved terahertz spectroscopy, *Opt. Express* **17**, 21969–21976 (2009).
31. Q. Wu and X. Zhang, Ultrafast electro-optic field sensors, **68**, 1995–1997 (1996).
32. G. Gallot and D. Grischkowsky, Electro-optic detection of terahertz radiation, *J. Opt. Soc. Am. B* **16**, 1204 (1999).
33. J. Blakemore, Semiconducting and other major properties of gallium arsenide, *J. Appl. Phys.* **53**, R123–R181 (1982).
34. *Fundamentals of Semiconductors – Physics and Materials Properties*, 3rd ed. (Springer, 2005).
35. H. C. Casey, D. D. Sell, and K. W. Wecht, Concentration dependence of the absorption coefficient for n- and p-type GaAs between 1.3 and 1.6 eV, *J. Appl. Phys.* **46**, 250–257 (1975).
36. M. Beard, G. Turner, and C. Schmuttenmaer, Transient photoconductivity in GaAs as measured by time-resolved terahertz spectroscopy, *Phys. Rev. B* **62**, 15764–15777 (2000).
37. Z. Mics, A. D'Angelo, S. A. Jensen, M. Bonn, and D. Turchinovich, Density-dependent electron scattering in photoexcited GaAs in strongly diffusive regime, *Appl. Phys. Lett.* **102**, 231120 (2013).
38. P. Kužel and H. Němec, Terahertz conductivity in nanoscaled systems: effective medium theory aspects, *J. Phys. D: Appl. Phys.* **47**, 374005 (2014).
39. R. Jacobsson, V light reflection from films of continuously varying refractive index, *Progress in Optics* **5**, 250–255 (1966).

1. Introduction

Time-domain terahertz (THz) spectroscopy (TDS) is a well-established method for the determination of optical properties (such as complex permittivity, conductivity, or refractive index) of materials and systems of interest in the THz spectral range [1–3]. Traditionally, THz spectroscopy relies on solid state-based emitters and detectors, such as e.g. nonlinear crystals, which are dispersive in both optical and THz spectral ranges. This leads to strict phase matching limitations in solid state-based THz generation and detection using ultrashort laser pulses.

THz air-photonics, in its turn, is based on nonlinear interaction of ultrashort laser pulses in air. As air has very little dispersion in both optical and THz ranges, the optical-THz phase matching limitation is conveniently lifted, thus permitting the generation and detection of ultra-broadband THz pulses with the frequencies well above 10 THz, and covering the entire THz spectral range without any gaps [4–8]. Many reports exist to-date on THz generation using dual-color laser induced air-plasma, and on THz detection using air-biased coherent-detection (ABCD) [4–11]. Yet, the implementation of THz air-photonics in accurate ultra-broadband THz spectroscopy of materials has remained challenging, and only very few reports exist on that matter [12–19]. The reason is that while THz air-photonics offers unparalleled possibilities such as the direct access to the entire THz spectral range in a single measurement and a very high (e.g. sub-50 fs) temporal resolution in transient THz spectroscopy, at the same time, it poses new challenges, also directly stemming from the ultrawide THz bandwidth available. Most THz spectrometers traditionally operate in transmission configuration, where the THz pulses interact with the volume of the material under study. The strength of the interaction can be then tuned by choosing the thickness of the sample, and as a result, highly accurate measurements can be performed (see e.g. [20]). However, this approach is less straightforward for ultra-broadband transmission-type THz spectroscopy, especially for arbitrarily thick samples, as most materials are opaque in the spectral range ca. 5–15 THz due to the presence of optically active lattice vibrations (see e.g. [13]). The advantage of the ultra-broad THz bandwidth available for spectroscopic measurements is thus lost. Consequently, the reflection geometry becomes a natural choice, as it allows one to utilize the *full bandwidth* of the THz pulse in the spectroscopic experiment. Yet to date it has only been rarely employed in transient THz measurements [15–19, 21–23], since such a configuration poses additional challenges as described below.

Since the interaction in reflection geometry takes place mainly at the surface of the sample, the interaction strength between the sample and the THz pulse is inherently low. As a consequence, both changes in amplitude and phase of the reflected THz pulse are small, and the retrieval of optical properties from reflection experiments is very sensitive to accurate measurements of the reflectivity phase, as pointed out already long time ago for steady-state measurements [24–27]; special precautions must be therefore taken to eliminate possible sources of phase errors [26]. Phase errors originate primarily from the displacement of the sample relative to the reference material. In transient THz spectroscopy, i.e. in a pump-probe experiment, this displacement is related to a long-term drift or jitter of the time-offset between the THz and gating optical branches. We note that a time offset τ as small as 3 fs (which corresponds to only 1 μm change in the optical path length) can significantly influence the inferred material response already for the frequencies around 1 THz [28]. Since the corresponding phase shift $\Phi = 2\pi\nu\tau$ is proportional to the probing frequency ν , the determination of the optical properties from reflection measurements at frequencies $\gtrsim 10$ THz critically requires the elimination of any possible source of the displacement between the THz and gating optical branches in the experiment. Figure 1 shows the difference between the real and inferred responses for $\pm 1 \mu\text{m}$ change in the optical path length between the THz pulse reflected respectively from the unexcited and from the photo-excited sample in optical pump-THz probe spectroscopy. While the real part of the conductivity shows only a reasonably small error due to the small fluctuation of the opti-

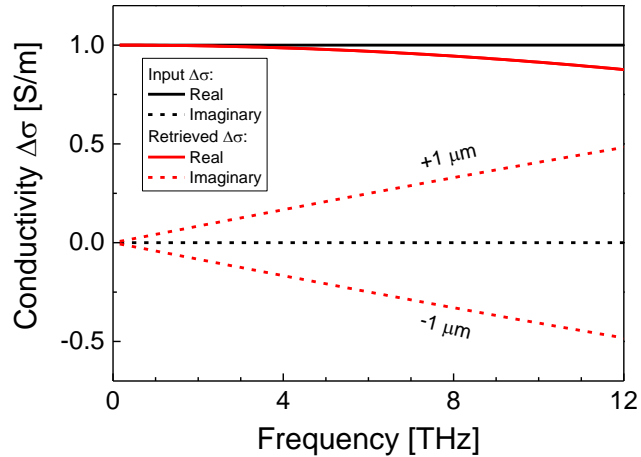


Fig. 1. Illustration of the influence of the phase error on the conductivity retrieved from transient reflectance. Black lines: model conductivity used to calculate transient reflectance spectra. Red lines: conductivity retrieved from the transient reflectance containing an artificial phase shift corresponding to $\pm 1 \mu\text{m}$ change in the optical path length between the THz reflected from the excited and unexcited sample. The minor micron-sized drift in the optical path can easily lead to wrong assignment of the conductivity mechanisms: the originally dispersion-free conductivity appears as a Drude response when a positive phase shift is artificially introduced, or it exhibits a signature of localization (negative imaginary part) when a negative phase shift is artificially introduced.

cal path, the error in the imaginary conductivity critically affects the physical interpretation of the photo-response. We note that similar effects also apply to the acquisition of transmission spectra of thin samples for which the sensitivity to the phase error may be comparable [29].

In this work, we developed a self-referenced technique for transient THz spectroscopy, specifically tailored for use with ultra-broadband THz air-photonics. In order to improve the phase stability in transient THz spectroscopy, and to suppress the effects of the long-term drift or jitter of the time-offset for optical pump-THz probe measurements (OPTP), Iwaszczuk *et al.* [30] proposed a self-referenced data acquisition scheme based on the double-modulation of both the optical pump and the THz probe using a dual-blade optical chopper. This experimental procedure ensures that both the reference (THz reflection from or transmission through the optically-unexcited sample) and the differential (optical pump-induced change in the THz reflectance or transmittance of the sample) signals are acquired simultaneously in one single scan, instead of comparing the two consecutive acquisitions separated by minutes or even hours of lab time. Since both the reference and the differential signals originate from the same pulse train and are acquired simultaneously, the effects of technical instabilities, such as timing jitter or laser power fluctuations, are drastically reduced. This method was specifically conceived for electro-optic sampling [31, 32] which directly detects a signal linear in the THz electric field. This scheme, however, cannot be straightforwardly applied to the THz air-photonics detection using ABCD [7], since obtaining a signal proportional to the THz field from ABCD would require an additional modulation step in the detection path.

The aim of this paper is twofold. (i) We demonstrate a self-referenced data acquisition method, taking advantage of the very nature of ABCD detection. It employs a specific modulation pattern of the optical pump pulses (by a conventional optical chopper), and of the electric bias switching sequence in the ABCD detection unit. This approach simultaneously provides the THz waveforms reflected from the unexcited and photoexcited sample at a chosen pump-

probe delay. (ii) We demonstrate that the commonly used approximation in THz data analysis, that of homogeneously excited film is in general insufficient for the correct retrieval of the optical properties from the reflectance spectra in ultra-broadband THz spectroscopy, and that its use can easily lead to unphysical spectral artifacts. The limits of validity of this popular approximation and the physical origin of its failure are analyzed. Our theoretical findings have been experimentally tested and verified using a thick semi-insulating GaAs wafer which exhibits a strong phonon absorption band around 8 THz [33], thus necessitating the use of the reflection geometry in the experiment. Additionally, the sensitivity to experimental errors is discussed. In this work, we present a rigorous method of ultra-broadband THz data analysis. Finally, for the weak signal limit, we derive an analytical expression for conversion of the measured transient THz reflectance into the quantity of interest, the complex-valued THz conductivity spectrum of the sample.

2. Self-referenced THz spectroscopy with ABCD detection

The schematic of our experimental setup is shown in Fig. 2(a). Additional details regarding our experimental setup can be found in [13]. The three arms of our THz spectrometer, namely the one for the THz generation, the THz detection (gating pulses), and the optical pumping are driven by 40 fs laser pulses of 800 nm wavelength from the amplified Ti:Sapphire laser operating at the repetition rate of $f = 1$ kHz.

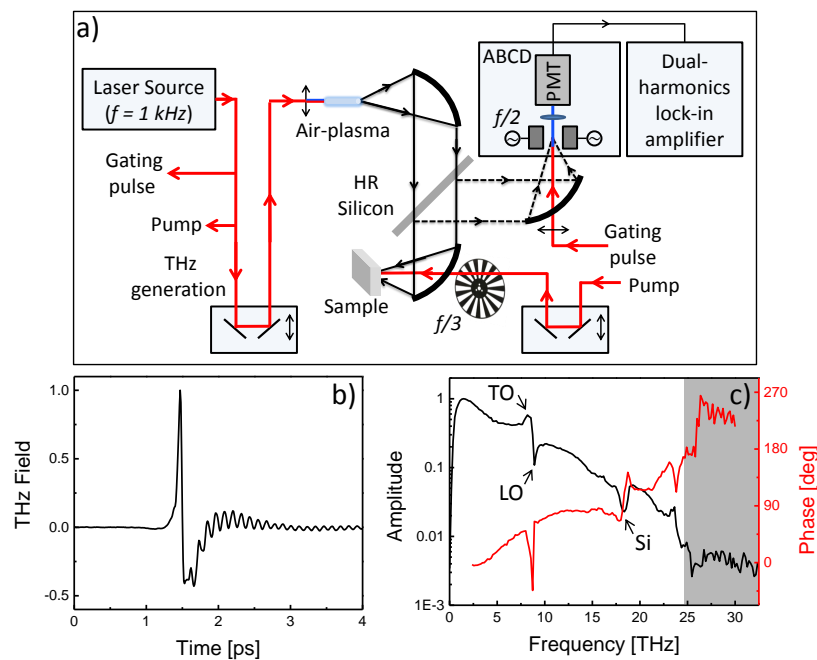


Fig. 2. a) Experimental setup for ultra-broadband self-referenced THz reflection spectroscopy based on THz air-photonics. b) THz pulse reflected from a 0.33 mm-thick GaAs wafer and normalized to the maximum. c) Corresponding amplitude and phase spectra. The arrows highlight spectral features originated respectively by the TO and LO phonon modes in the GaAs [33] sample and by the two-phonon absorption in the high resistivity silicon beam splitter [34]. The shaded area indicates the spectral region corresponding to the noise floor of the signal.

Ultrashort quasi single-cycle THz transients are generated by dual-color frequency mixing in air-plasma [4, 9]. A high-resistivity silicon wafer is employed as ultra-broadband THz beam splitter. The THz pulse impinges on the sample under normal incidence and the THz beam reflected from the sample is then detected using the ABCD detector. The excitation beam width was more than ten times larger than the THz spot size, ensuring a homogeneous lateral excitation profile. Figure 2(b) shows a THz pulse acquired with our experimental setup when a thick (0.33 mm) GaAs wafer is used as a sample. Spectral information is obtained by means of a numeric FFT calculation which provides both the amplitude and the phase spectra of the reflected THz pulse (Fig. 2(c)).

In our experiment we use a double-modulation approach [15–18, 30] with a specific modulation pattern. The first modulation channel at the frequency of $f/3$ is provided by an optical chopper, designed to transmit only one every third pump pulse as shown in Fig. 3(a). The second modulation channel is provided by the ABCD detection unit itself: the modulation is achieved by switching the high voltage bias in the ABCD detector unit, which is supplied by a square wave oscillating between $V = \pm 1.6$ kV, at the frequency of $f/2$. Under the presence of the electric field (bias plus THz electric field), the second-harmonic (SH) of the near-infrared gating pulse is generated and measured using a photo-multiplier tube (Fig. 3(b)). A dual-harmonic lock-in amplifier (AMETEK 7270) permits the simultaneous acquisition of the photo-multiplier tube (PMT) output signal at two sub-harmonic frequencies: at the frequency $f/6$, which becomes the fundamental modulation frequency in this measurement as explained below, and at its third harmonic $f/2$. We show below that these two modulation steps are sufficient to extract a signal that is linear in the THz field, although the SH generation of the gating laser pulse is a $\chi^{(3)}$ process which is quadratic in the total applied field [7]. We note that this detection method is intrinsically different from the more conventional electro-optic sampling, which directly provides a signal linear in the THz field.

For the experimental conditions shown in Fig. 3(b), the intensities of the second harmonic can be written as:

$$I_{0,e}^{\pm} \propto \left| \chi^{(3)} I_{\omega} (E_{0,e} \pm E_{bias}) \right|^2, \quad (1)$$

where $\chi^{(3)}$ is the third-order non-linear susceptibility of air and I_{ω} is the near-infrared gating pulse intensity. The subscripts and superscripts in Eq. (1) are used to describe the four possible SH intensities which are marked with the distinct colored circles in Fig. 3(b). During one period of the fundamental frequency $f/6$ we encounter four different signals ($I_0^+, I_e^+, I_0^-, I_e^-$): the THz pulse probes either the unexcited sample E_0 (green) or the excited sample E_e (red); and this is combined with either of the two high voltage bias polarities at ABCD unit, a positive $+E_{bias}$ (dashed red/green) or negative polarity (solid red/green). In the following we refer to the signals generated from the same THz field but under opposite ABCD bias, as twin-signals. Namely (I_0^+, I_0^-) and (I_e^+, I_e^-) are the two pairs of twin-signals, which can be recognized in Fig. 3(b) by the pairs of circles with the same color but different line styles.

A quick inspection of Eq. (1) reveals that the SH intensities contain not only the heterodyne signal (simply proportional to the THz field) but also an offset and a term quadratic in the THz field. The two latter spurious components can be eliminated using appropriate lock-in detection, which is the core of our self-referenced acquisition scheme (Figs. 3(b) and 3(c)). The input signal of the dual harmonic lock-in amplifier is formed by the vectorial sum of six phase-shifted components repeated with the fundamental frequency of $f/6$ (Fig. 3(b)). From simple algebraic considerations we find that the heterodyne detection signals corresponding to the THz fields can be obtained by summing the twin-signals in the mutual phase opposition:

$$E_{0,e} \propto (I_{0,e}^+ - I_{0,e}^-). \quad (2)$$

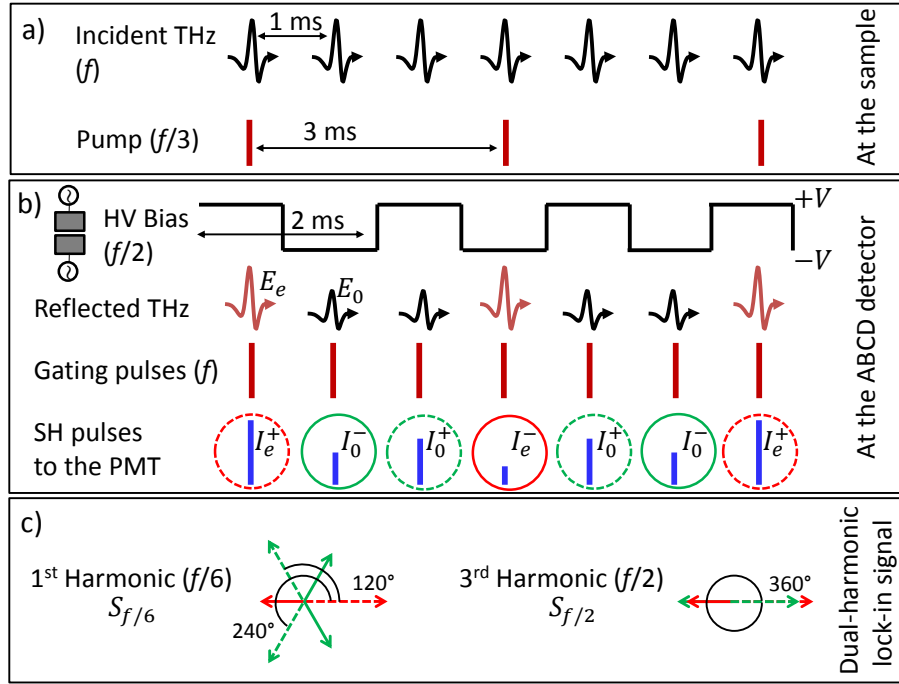


Fig. 3. Self-referenced acquisition scheme for ABCD detection. a) THz and pump pulses impinging on the sample. b) From the top to the bottom: High-voltage electric bias; THz pulse reflected from the excited (red) and unexcited (black) sample; incident gating pulses (red); second harmonic pulses (blue) in the ABCD detection. Couples of twin-signals (dashed/solid lines of the same color) are circled in red and green for the THz pulse reflected from the excited and unexcited sample respectively. c) Signals detected in the lock-in amplifier when the reference frequencies are respectively $f/6$ and $f/2$. Twin-signals (dashed/solid lines of the same color) are 180° out of phase and their vector sum is linearly proportional to the THz field (Eq. (2)).

When the lock-in reference is set to $f/6$, the input signal can be decomposed into three couples of twin-signals satisfying Eq. (2) where each couple contributes by one third to the overall signal. This relation is illustrated in Fig. 3(c) by the pairs of opposite vectors colored with two different shades of red and green, respectively, for the THz pulse reflected from unexcited and excited sample. The sum of signals marked in red gives rise to the heterodyne signal proportional to E_e and the sum of those in green is proportional to E_0 . The overall signal at $f/6$ is proportional to the differential THz waveform:

$$S_{f/6} = k [(I_e^+ - I_e^-) - 0.5(I_0^+ - I_0^-) - 0.5(I_0^+ - I_0^-)] \propto (E_e - E_0). \quad (3)$$

where k is a factor determined by the PMT and the lock-in amplifier instruments. To achieve self-referenced detection, the pure reference signal must be also acquired from an independent linear combination of E_0 and E_e . The latter can be obtained by demodulating the signal at $f/2$. As shown in Fig. 3(c) the input signal at $f/2$ can be decomposed into three couples of in-phase twin signals yielding:

$$S_{f/2} = k [2(I_0^+ - I_0^-) + (I_e^+ - I_e^-)] \propto (2E_0 + E_e). \quad (4)$$

The reference THz signal E_0 can be then easily reconstructed from Eqs. (3) and (4).

To provide an experimental proof of our self-referenced spectroscopy method, we have characterized an undoped 0.33 mm-thick GaAs wafer photoexcited at 800 nm at room temperature. GaAs is an archetypical ionic semiconductor, widely used in electronics, with a direct bandgap of 1.4 eV and a Drude-like photoconductivity response [35–37]. To illustrate the operation of our demodulation method, we performed a 1D-pump scan [36] with the THz delay line fixed at the peak value of the THz probe signal, and the optical pump being time-delayed (Fig. 4). For negative pump-probe delays the average differential signal $S_{f/6}$ is zero since there is no photo-induced change in the response function of the sample. Immediately after photo-excitation, the reconstructed THz peak amplitude reflected from the excited sample E_e rapidly rises to its maximum value, and then it slowly returns to the equilibrium level as the differential signal approaches zero, precisely as expected (Fig. 4). At the same time, the reconstructed reference signal E_0 , corresponding to the THz pulse reflected from the unexcited sample, does not change upon photo-excitation for all pump-probe delays (Fig. 4), also in perfect agreement with the expectations. As a result, the demonstrated double-modulation technique, using a simple chopper for optical pump modulation and a natural bias-switching sequence in the ABCD unit for THz detection modulation, allows one to simultaneously acquire the THz signals reflected from the unexcited and the photoexcited samples.

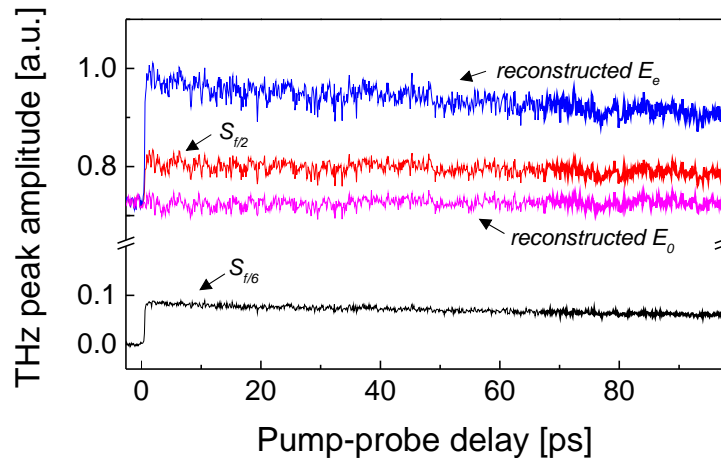


Fig. 4. Self-referenced acquisition of a 1D-pump scan at the peak of the THz field for a GaAs wafer excited at 800 nm with a pump fluence of 0.35 mJ cm^{-2} . Lines in black and red are the simultaneously acquired signals $S_{f/6}$ and $S_{f/2}$ respectively. Lines in blue and magenta are respectively the reconstructed reference and differential THz waveforms obtained by using Eqs. (3) and (4).

3. Analysis of transient reflectance spectra

In this section we concentrate on the analysis of transient reflectance spectrum in the frequency domain. We assume a thick bulk sample, such that all multiple internal reflections of a probing THz pulse can be simply separated by the temporal windowing. One face of the sample is optically excited and all the pump pulse energy is absorbed within the sample (i.e. excitation density at the sample output face vanishes). Note that in our analysis we do not impose the approximation that the photoexcited layer is thin compared to the THz wavelength. In reflection geometry the principal measurable quantity is the complex transient reflectance spectrum:

$$\frac{\Delta r}{r_0} \equiv \frac{E_e - E_0}{E_0}, \quad (5)$$

where $r_0 = (1 - n_0)/(1 + n_0)$ is the sample reflectivity without photo-excitation and n_0 is the complex frequency-dependent refractive index of the unexcited sample at THz frequencies.

In order to calculate Δr induced by the photo-excitation, one should solve the wave equation with a prescribed depth profile of the transient conductivity $\Delta\sigma(z)$. This can be done analytically in the limit of the small signal ($\Delta r \ll r_0$). The calculation is described in the Appendix and it yields a general expression (18) valid for any sample thickness and any conductivity profile $\Delta\sigma(z)$. In our special case of a bulk sample, where multiple internal reflections can be removed, this formula can be simplified:

$$\frac{\Delta r}{r_0} \approx \frac{2Z_0}{n_0^2 - 1} \cdot \int_0^L \Delta\sigma(z) \exp\left[\frac{2i\omega n_0 z}{c}\right] dz, \quad (6)$$

where Z_0 is the wave impedance of vacuum, L is the sample thickness, and c is the speed of light in vacuum. It should be noted that in an analogous formula for the transmission geometry [38], the exponential term in Eq. (6) is absent in the argument of the integral. In other words, in the limit of small signal the measured differential transmittance $\Delta t/t_0$ is simply proportional to the transient *sheet* conductivity $\Delta\Sigma$, *independent* of the particular depth profile of the excitation density:

$$\frac{\Delta t}{t_0} \propto \Delta\Sigma \equiv \int_0^L \Delta\sigma(z) dz. \quad (7)$$

The difference between Eqs. (6) and (7) is very important and, consequently, the analysis of transient transmission and reflection signals must be also different. In the transmission geometry all the photo-generated charges contribute to the differential signal *in phase*, which means that their spatial distribution in the z direction does not play any role if their response is linear in THz field (the most usual case). By contrast, in the reflection geometry the contributions of various photoexcited layers of the sample are mutually *dephased*. This represents an intrinsic complication: inappropriate analysis of the data may generate an additional phase error, easily leading to a physical misinterpretation of the nature of photoconductivity (see Fig. 1 and discussion in the Introduction). That is, the reflectance is strongly sensitive to the particular profile of the excitation density.

The profile of the excitation density may acquire various forms; the most common case (that of e.g. homogeneous semiconductors photoexcited in the linear regime) is an exponential excitation profile given by the Lambert-Beer absorption law:

$$\Delta\sigma(z) = \Delta\sigma_s \exp[-\alpha z]. \quad (8)$$

In this case Eq. (6) yields:

$$\frac{\Delta r}{r_0} = \frac{2Z_0}{n_0^2 - 1} \cdot \frac{\Delta\sigma_s}{\alpha} \cdot \frac{1}{1 - \frac{2i\omega n_0}{\alpha c}}, \quad (9)$$

where α is the linear optical pump absorption coefficient ($\alpha L \gg 1$) and $\Delta\sigma_s$ is the photoconductivity at the surface of the slab.

It should be noted that the differential reflectance Eq. (6) assumes the form analogous to the differential transmittance Eq. (7) *only* when the thickness $d = 1/\alpha$ of the photoexcited part of the sample is much smaller than the shortest wavelength of the broadband THz radiation ($2\omega n_0 d/c \ll 1$), in the so-called thin-film approximation (TFA):

$$\frac{\Delta r}{r_0} \approx \frac{2Z_0}{n_0^2 - 1} \cdot \Delta\Sigma, \quad (10)$$

where $\Delta\Sigma = \Delta\sigma_s/\alpha$ in the case of the exponential excitation profile (Eq. (9)). In many theoretical models, a step-like excitation approximation (SEA) is also used. In this approximation the spatial dependence of the photoexcited layer is neglected and a homogeneous conductive layer with thickness $1/\alpha$ is considered. The transient reflectance in Eq. (6) then reads:

$$\frac{\Delta r}{r_0} = \frac{2Z_0}{n_0^2 - 1} \cdot \frac{\Delta\sigma_s}{\alpha} \cdot \frac{\exp\left[\frac{2i\omega n_0}{\alpha c}\right] - 1}{\frac{2i\omega n_0}{\alpha c}}. \quad (11)$$

In a truly thin-film excitation limit both Eqs. (9) and (11) reduce to the same form Eq. (10). For thicker excited layers, Eq. (10) loses its validity while Eq. (11) does not properly account for the profile of the excitation density. We illustrate these results on a calculation of a differential reflectance of a photoexcited GaAs wafer under normal incidence.

We consider an exponential excitation profile given by $\alpha = 1.3\mu\text{m}^{-1}$ which corresponds to the linear absorption in GaAs at 800 nm [33, 35] and the dispersion of the unexcited GaAs including the strong phonon mode at $\nu_{TO} = 8.04\text{ THz}$, with $n_0 = \sqrt{\epsilon}$, where ϵ is the complex-valued dielectric function $\epsilon = \epsilon_\infty + \nu_{TO}^2(\epsilon_0 - \epsilon_\infty)/(\nu_{TO}^2 - \nu^2 + i\gamma\nu)$. Here ϵ_0 is the static permittivity, ϵ_∞ is the high-frequency contribution to the permittivity of GaAs, and γ is the damping constant of the lattice oscillation [33]. The response of the photoexcited carriers is modeled by a Drude term: $\Delta\sigma_s = \Delta\sigma_{dc}/(1 - i2\pi f\tau_s)$ with $\tau_s = 250\text{ fs}$ [25, 36, 37] and $\Delta\sigma_{dc} = 1\text{ S m}^{-1}$. The photoconductivity is chosen such that $\Delta r/r_0 < 1\%$. First we calculated the reflectance of an excited sample by numerical solution of Maxwell's equations in a medium inhomogeneous along z ; for this we used the transfer matrix method for inhomogeneous media method described

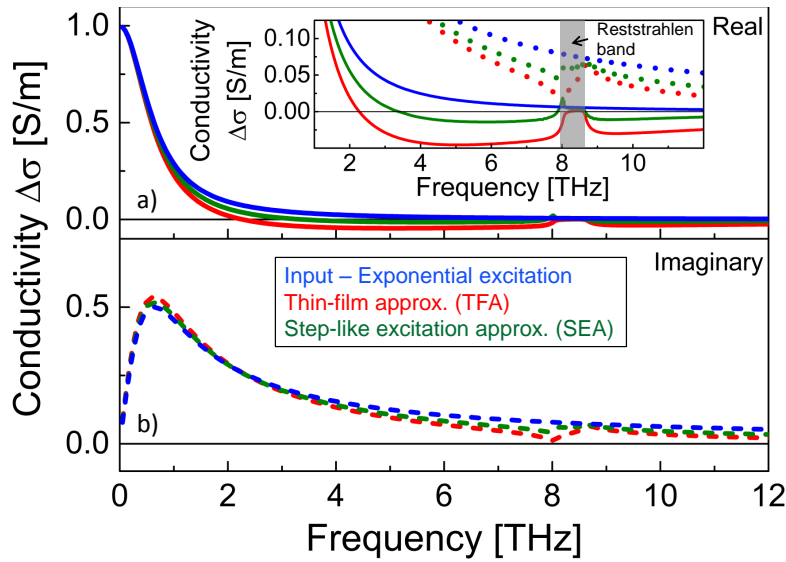


Fig. 5. Real (solid, a) and imaginary (dashed, b) parts of the photoconductivity of a GaAs wafer retrieved within various approximations. Blue curves: input Drude-like conductivity used to calculate the transient reflectivity. Red and green curves are erroneous conductivities calculated respectively using TFA (Eq. (10)) and SEA (Eq. (11)). The conductivity retrieved using Eq. (9) exactly matches the blue curve in the plot. Inset: zoom of the real and imaginary parts of the calculated photoconductivities.

in [39] which transforms the problem to the solution of an ordinary differential equation. From that we deduced the differential reflectance spectra $\Delta r/r_0$. Next, we inverted Eqs. (9)-(11) to retrieve the photoconductivities within these approximations. The results are summarized in Fig. 5.

The thin film approximation (TFA), Eq. (10), considerably deviates from the correct result, already at frequencies just above 1 THz (for the optical penetration depth of $1/\alpha = 0.7 \mu\text{m}$). Indeed the relative deviation of the thin-film approximation is about $|2k/\alpha|$, where $k = \omega n_0/c$ (cf. Eqs. (9) and (10)). The results obtained by SEA using Eq. (11) are marginally better, but the agreement with the correct curve is still relatively poor. Finally, Eq. (9) correctly retrieves the properties of photoexcited GaAs, proving the point that the knowledge of the excitation profile is crucial for the accurate analysis of the transient reflectance spectra. Note how an inappropriate use of TFA or SEA may lead to unphysical results, such as a negative-valued real conductivity in absorbing media (inset of Fig. 5). We also observe that the conductivity spectrum retrieved using inappropriate approximations is strongly distorted in the vicinity of the TO and LO phonon modes where it shows a clear artifact (inset of Fig. 5). Indeed, the equilibrium reflectance r_0 is quite high in this spectral range, making the data especially sensitive to experimental errors.

It should be noted that the penetration depths up to $\sim 0.1 \mu\text{m}$ are short enough to enable the application of the TFA in the low THz range. Further, the use of higher energy pump photons usually leads to shorter penetration depths. However, we have to keep in mind that such a shorter penetration depth can be considered in the evaluation of the spectra only if the photo-carrier diffusion is negligible (this is the case for short pump-probe delays and/or low-mobility materials). If the carrier diffusion is important, Eq. (6) should be used with the appropriate depth profile of carrier concentration [36, 37].

In the following part we illustrate the sensitivity of the retrieved transient conductivity to experimental errors on a particular case of the finite time-domain scan length. The frequency resolution in the time-domain spectroscopy is $1/(2T)$ where T is the length of the acquisition time-window; in other words, the frequency cannot be determined with an accuracy better than

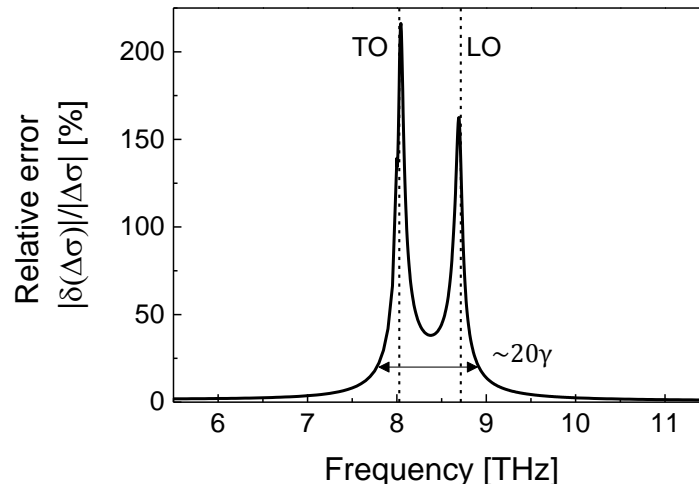


Fig. 6. Error in the transient conductivity due to a frequency uncertainty $\delta\nu$ of 0.05 THz corresponding to a 10 ps time window.

$1/(2T)$. The error in the conductivity $\delta(\Delta\sigma)$ due to an uncertainty of the frequency $\delta\nu$ reads:

$$\delta(\Delta\sigma) = \frac{\partial(\Delta\sigma)}{\partial(\Delta r/r_0)} \cdot \underbrace{\frac{\partial(\Delta r/r_0)}{\partial\nu}}_{\delta(\Delta r/r_0)} \cdot \delta\nu. \quad (12)$$

An example of this error is shown in Fig. 6. Close to a sharp TO phonon-mode and in the reststrahlen band between TO and LO modes the amplitude of the differential reflectance is strongly reduced since r_0 is saturated and the plasma oscillations of photo-carriers cannot couple directly to the transverse mode of the lattice. As a consequence the first term of the product at the right-hand-side of Eq. (12) diverges and any minor error of the transient signal $\delta(\Delta r/r_0)$ is thus strongly amplified when the transient conductivity is calculated. As the LO phonon frequency f_{LO} is approached, a sharp peak appears in the measured differential reflectivity as a sign of the interaction between the free carrier oscillations and the LO vibration of the lattice. As a result the second term at the right-hand-side of (12) diverges, leading to a large error in the conductivity retrieved around the LO phonon mode.

It should be noted that the frequency and its uncertainty appearing in Eq. (12) can be replaced by any other relevant physical quantity and its corresponding uncertainty, such as, for instance, the refractive index of the unexcited sample n_0 and its uncertainty δn_0 . Thus, even if the refractive index of GaAs is a well-known parameter, its minor uncertainty can also produce non negligible errors especially in the spectral region around the sharp phonon mode. This is indeed a good additional reason to exclude the frequencies around the reststrahlen band from the reliable spectral window of transient THz spectroscopy experiment.

Let us return to the time-resolved reflectance experiments with an undoped 0.33 mm-thick GaAs wafer photoexcited at 800 nm, and apply the analysis approaches described above to measured data. The THz reflectance spectrum was acquired at 3.5 ps after photo-excitation, using the double-modulation self-referenced technique as described in Sec. 2. The resulting transient conductivities retrieved using the three analysis approaches: general analysis approach using the spatially-distributed excitation profile Eq. (9), TFA Eq. (10), and SEA Eq. (11), are shown in Fig. 7. The data points around the reststrahlen band have been discarded because of larger relative error as illustrated in Fig. 6. The conductivity retrieved by the general approach Eq. (9) (blue points in Fig. 7) was successfully fitted using a Drude model. The Drude fitting parameters provide values of the carrier relaxation time of 0.09(1) ps and of the carrier density $6(1) \times 10^{16} \text{ cm}^{-3}$. The Drude carrier concentration is in reasonable agreement with the density of absorbed photons ($\sim 9 \times 10^{16} \text{ cm}^{-3}$). The inferred scattering time is consistent with the value of 0.10(1) ps obtained using conventional transmission THz spectroscopy in the frequency range 0.2–2.5 THz under the same excitation conditions.

Note also that Eq. (6) is valid only for small signals. For larger signals, the relative error of the linear approximation is of the order of $|\Delta R/R|$, i.e., a signal with amplitude $|\Delta R/R|$ of 5% causes approximately 5% error in $\Delta\sigma$. Finally, it should be noted that broadband THz spectroscopy is more sensitive to conductivity contributions characterized by shorter carrier momentum scattering times. It can be thus highly suitable for the investigation of low-mobility semiconductors such as e.g. CdS or ZnO. For the case of high-mobility semiconductors such as GaAs, it may be possible to distinguish further contributions on top of the main Drude response, which may indicate e.g. the presence of a distribution of scattering times [36]. In this sense, ultra-broadband reflection-mode THz spectroscopy paves the way towards much better understanding of fine details of charge transport in electronic materials.

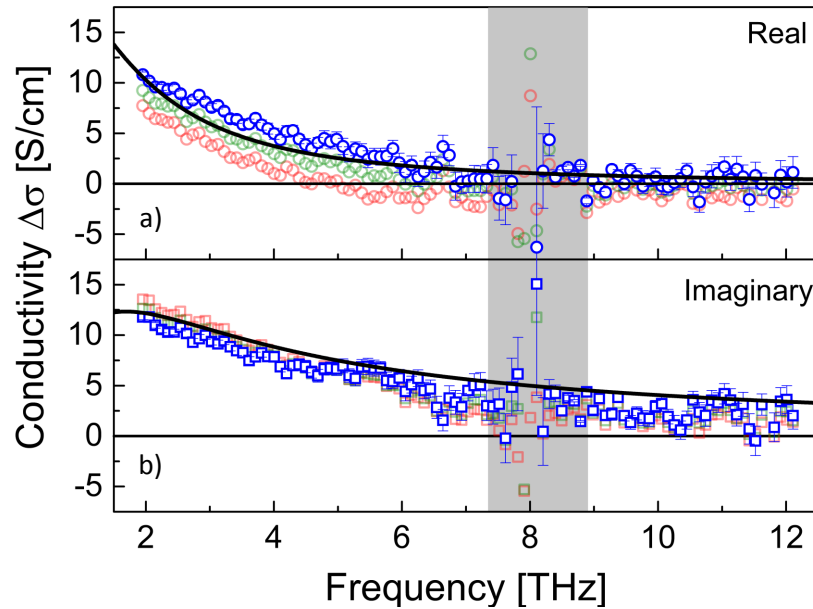


Fig. 7. Real (a) and imaginary (b) parts of the transient conductivity calculated by using TFA (red), SEA (green), and by taking into account the exponential excitation profile (blue). Black curves: Drude fit of the reliable conductivity data. The parameters of the Drude fit are: $N = 6(1) \times 10^{16} \text{ cm}^{-3}$ for the carrier density and $\tau = 0.09(1) \text{ ps}$ for the scattering time. The transient reflectivity was measured 3.5 ps after photo-excitation and for an average excitation energy of $3 \mu\text{J cm}^{-2}$ per pulse. The error bars have been estimated as the standard error of the mean over 61 individual acquisitions.

4. Conclusion

We have provided general guidelines for ultra-broadband transient THz spectroscopy with THz air-photonics. We developed the novel double-modulation technique specifically tailored towards using with air-based coherent detection (ABCD), which allows for self-referenced transient spectroscopy with minimal phase error over the entire ultra-broad bandwidth of the air-photonics THz signals. We have provided an accurate conductivity retrieval approach, which requires knowledge of the spatial distribution of the photo-carriers within the sample. This has an important implication especially for experiments carried out at long pump-probe delays where the initial exponential depth profile of the photocarrier distribution may substantially expand and change its shape due to the diffusion [37].

For a small-signal regime, a convenient analytical expression Eq. (9) was developed, linking the THz photo-reflectivity and THz photoconductivity. At the same time, we have demonstrated that the use of popular approximations, such as TFA or SEA, is likely to result in false (and also unphysical) features in the recovered photoconductivity spectra. The applicability criteria of these approximations were discussed. We have provided the estimate of the relative error in the measured photoconductivity, caused by the spectrally sharp features in the background dielectric function of the material, such as phonon modes. Our experimental protocol and the developed data analysis approach was successfully verified using the transient THz spectroscopy on GaAs, an archetypal material for this class of experiments.

Appendix

In this appendix we derive a general expression for the transient reflectance under normal incidence of a photoexcited sample in a weak signal approximation, i.e. $\Delta E \ll E$, where E is the field which propagates in the sample in equilibrium and ΔE is the field change due to photoexcitation. Similar derivation for the transient transmitted field has been published recently [38] and in this work we follow the same method of analysis. The photo-induced field $\Delta E(z)$ inside the sample (Fig. 8) obeys the following wave equation:

$$\frac{d^2 \Delta E(z)}{dz^2} + k^2 \Delta E = -ik_0 Z_0 \Delta j(z) \quad (13)$$

where Z_0 is the vacuum wave impedance, $k_0 = \omega/c$ is the vacuum wave vector of the THz field, $k = n_0 k_0$, $\Delta j(z) = \Delta \sigma(z) E(z)$ and z is the spatial coordinate perpendicular to the sample surface (Fig. 8).

The complex photoconductivity $\Delta \sigma(z)$ may have a general depth profile: it can simply follow the Lambert-Beer absorption law expressed by Eq. (8) or it can be substantially modified e.g. by non-percolated parts of the sample or by the carrier diffusion [37, 38]. Equation (13) is linear, therefore its solution inside the sample reads:

$$\Delta E(z) = \delta \exp(-ikz) + \gamma \exp(ikz) + G(z), \quad (14)$$

where $G(z)$ is the particular solution of the wave equation with the right-hand-side:

$$G(z) = \frac{Z_0}{2n_0} \left[\exp(-ikz) \int_0^z \Delta j \exp(ikz) dz - \exp(ikz) \int_0^z \Delta j \exp(-ikz) dz \right]. \quad (15)$$

The continuity conditions of the electric field $\Delta E(z)$ and of the magnetic field

$$\Delta H(z) = \frac{ic}{\omega Z_0} \frac{d\Delta E}{dz} \quad (16)$$

must be satisfied at the input and output surface of the sample:

$$\begin{aligned} \Delta E(0) &= \Delta E_r, & \Delta H(0) &= \Delta H_r, \\ \Delta E(L) &= \Delta E_t, & \Delta H(L) &= \Delta H_t. \end{aligned} \quad (17)$$

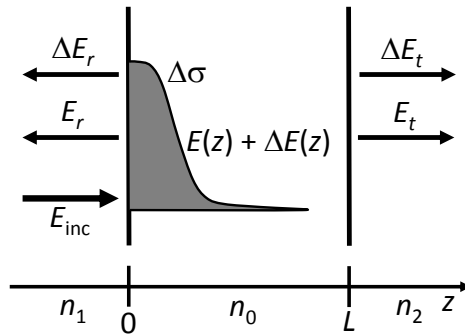


Fig. 8. Scheme of fields and interactions in a photoexcited sample during transient transmittance ΔE_t and transient reflectance ΔE_r measurements. In equilibrium, the incident THz field E_{inc} and the transmitted E_t and reflected E_r fields fulfill standard Fresnel equations.

These four equations allow one to determine the constants δ and γ and the transient output fields ΔE_r and ΔE_t . One finds:

$$\begin{aligned} \Delta E_r = & -\frac{Z_0 t_1^2 a^2}{2n_1} \left[\int_0^L \exp(2ikz) \Delta \sigma(z) dz + \right. \\ & + 2r_2 \exp(2ikL) \int_0^L \Delta \sigma(z) dz + \\ & \left. + (r_2 \exp(2ikL))^2 \int_0^L \exp(-2ikz) \Delta \sigma(z) dz \right], \end{aligned} \quad (18)$$

cf. Eq. (42) in [38]. Here $t_1 = 2n_1/(n_0 + n_1)$ is the transmission coefficient of the input sample surface and $r_2 = (n_0 - n_2)/(n_0 + n_2)$ is the internal reflection coefficient at the output sample surface. The parameter a describes multiple internal reflections of the THz beam inside the sample:

$$a = [1 - r_1 r_2 \exp(2ikL)]^{-1}, \quad (19)$$

where $r_1 = (n_0 - n_1)/(n_0 + n_1)$. In particular, for a thick sample, where the photoexcited part is much thinner than the total sample thickness and where multiple internal reflections in the time-domain wave form can be removed by the windowing procedure, we can simply consider the unexcited part of the sample as the substrate, i.e. $n_0 \equiv n_2$ and $r_2 = 0$, $a = 1$. In this case we obtain a very simple formula which will be used in the main part of the paper:

$$\frac{\Delta r}{r_0} \equiv \frac{\Delta E_r}{E_r} = \frac{2Z_0 n_1}{n_0^2 - n_1^2} \int_0^L \exp(2ikz) \Delta \sigma(z) dz. \quad (20)$$

Acknowledgments

This work was financially supported by the European Commission (EU Career Integration Grant #334324 LIGHTER), the Czech Science Foundation (Grant 13-12386S), and the Max Planck Society. We are grateful to Z. Mics, I. Ivanov, and D. G. Cooke for helpful discussions.